Springer Acta Mechanica Sinica

•RESEARCH PAPER•

Acta Mech. Sin., Vol. 38, 222108 (2022)
https://doi.org/10.1007/s10409-022-22108-x

The scaling of charging rate and cycle number of commercial batteries

Jici Wen[1,4†], Qingrong Zou[2†], Zehui Zhang[1,4], Jian Shi[3,5], and Yujie Wei[1,4*]

[1] State Key Laboratory of Nonlinear Mechanics, Institute of Mechanics, Chinese Academy of Sciences, Beijing 100190, China;
[2] School of Applied Science, Beijing Information Science and Technology University, Beijing 100192, China;
[3] Academy of Mathematics and Systems Science, Chinese Academy of Sciences, Beijing 100190, China;
[4] School of Engineering Sciences, University of Chinese Academy of Sciences, Beijing 100049, China;
[5] School of Mathematical Sciences, University of Chinese Academy of Sciences, Beijing 100049, China

Received April 7, 2022; accepted April 25, 2022; published online May 12, 2022

Health management for commercial batteries is crowded with a variety of great issues, among which reliable cycle-life prediction tops. By identifying the cycle life of commercial batteries with different charging histories in fast-charging mode, we reveal that the average charging rate c and the resulted cycle life N of batteries obey $c = c_0N^b$, where c_0 is a limiting charging rate and b is an electrode-dependent constant. This c-N law, resembling the classic stress versus cycle number relationship (the S-N curve or Wohler curve) of solids subject to cyclic loading, could be applicable to most batteries. Such a scaling law, in combination with a physics-augmented machine-learning algorithm, could foster the predictability of battery life with high fidelity. The scaling of charging rate and cycle number may pave the way for cycle-life prediction and the directions of optimization of advanced batteries.

Cycle-life law, *c*-*N* fatigue, Charging rate, Lithium-ion battery, Electro-chemo-mechanical coupling

Citation: J. Wen, Q. Zou, Z. Zhang, J. Shi, and Y. Wei, The scaling of charging rate and cycle number of commercial batteries, Acta Mech. Sin. **38**, 222108 (2022), https://doi.org/10.1007/s10409-022-22108-x

1. Introduction

There is practical wisdom that engineering systems in cyclic service often fatigue and may fail catastrophically by accumulated damage originating at small scales not easy to discern. An analogous mechanism is also encapsulated in rechargeable batteries. Taking a lithium-ion battery (LIB) for illustration, the electrode material experiences expansion during lithiation as lithium atoms are forced to flow in, and a constrained boundary will introduce internal compressive stress on average; delithiation gives rise to tensile stress in the opposite. A complete working cycle of a LIB produces a reversal of stress status, but something has changed perpetually because the system is different from its original state on the microscopic perspective. Existing experimental observations indeed supply a strong correlation between electrochemical degradation and mechanical failure. Electrochemically induced fracture in electrodes has been clearly seen [1,2]. Those electrochemically induced cracks, propagated during charge and discharge cycling, can cause capacity performance degradation in LIBs by active material shedding [3], the loss of electrical contact [2], lithium loss by SEI formation in the accumulative exposure of crack surfaces [4], and so on.

However, while the degradation of charge-discharged batteries resembles and originates from damage evolution in cyclically stressed structural materials, it is far more intriguing to come up with a cycle-life prediction for the former. Fatigue in batteries involves strongly electro-chemo-mechanical coupling, and ought to be a process of multiple interwoven factors. Environmental factors like the charging mode and serving history kick in to alter the charging performance of batteries and thereafter their cycle life. A straightforward parameter like stress in structural materials for the application of S-N curves is not accessible [5-7].

---

†These authors contributed equally to this work.
*Correspondence author. E-mail address: yujie_wei@lnm.imech.ac.cn (Yujie Wei)
Executive Editor: Haosen Chen

Singling out parameters for life assessment of chargeable batteries is so far under exploration [8-10]. Many key issues, including the evolution of electrode structure and active material [3,11-17], solid-electrolyte interphase [4,18,19], interfacial contact and resistance [20,21], and so on, have been examined in depth. Regardless of the tremendous progress on identifying possible mechanisms responsible for performance degradation, the interwoven mechanisms often obscure the full picture of the failure process.

In the way to build up a holistic approach to identifying those interweaving factors accounting for battery life, we aim to find a physically sound yet pragmatic metric for the cycle life of batteries by putting aside other issues. Among the list of fatigue-related factors, changing rate tops for the commercial competitiveness of batteries [22-26]. Long charging time of LIBs, even up to several hours, seriously restricted its widespread adoption of electric vehicles (EVs) when competing to the refueling time (often 5-10 min) in gasoline-powered vehicles [27]. The tradeoff between fast-charging and cycle life stimulates broad interest among researchers to explore possible fast-charging protocols for the long cycle-life performance of LIBs, in parallel to endeavors to seek better anode and cathode materials [1,28,29]. It is our purpose here to (1) reveal a scaling of cycle life of batteries with one experimentally controllable parameter (fast-charging rate) and to (2) supply accurate cycle-life estimation of an individual cell with minimum testing data by using the finding of (1) and its combination with a physics augmented-machine learning (PA-ML) algorithm.

2. The charging rate versus cycle number in battery fatigue

We firstly performed a comprehensive literature review on experimental investigation for charging rate and the number of cycles in commercial batteries, mainly from Severson et al. [30,31]. The authors reported a total of 169 tests on commercial LFP/graphite A123 LIBs. We show in Fig. 1a a typical fast-charging mode with a multi-stage current in different states of charge S_c, and the corresponding voltage-S_c curve is given in Fig. 1b. The charging protocol contains four stages (3.6 C for $S_c \leq 20\%$, 6.0 C for $S_c \leq 40\%$, 5.6 C for $S_c \leq 60\%$, and 4.8 C for $S_c \leq 80\%$), followed by a slow

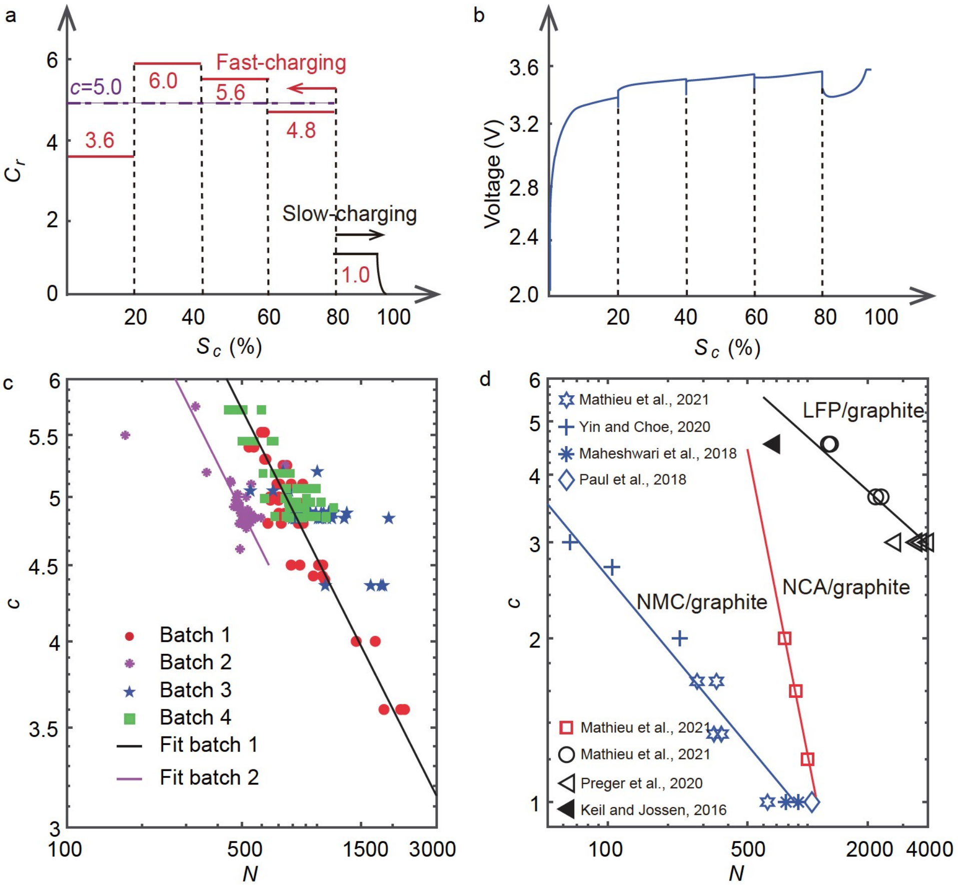

Figure 1 Average charging rate *c* and the resulted cycle number *N* of LIBs. **a** A typical multi-stage charging protocol and **b** its corresponding voltage-S_c curve. **c** *c*-*N* relationship and the fitting results (solid lines) using Eq. (1). Symbols are experimental data from Severson et al. [30,31], see Table S5. **d** *c*-*N* curves of three types of commercial LIBs with different electrodes, with symbols from experiments and lines using Eq. (1). We here set the cycle life as the battery's maximum capacity falling to 70% for NMC/graphite LIBs, 50% for NCA/graphite LIBs, and 80% LFP/graphite LIBs from the capacity retention curve (NMC: $LiNi_{0.8}Mn_{0.1}Co_{0.1}O_2$, NCA: $LiNi_{0.8}Co_{0.15}Al_{0.05}O_2$, and LFP: $LiFePO_4$, see Table S6).

constant current (CC, 1 C)-constant voltage (CV, 3.6 V) charging mode till $S_c = 1$. In the valuable experiments, the authors designed four batches of tests with distinct fast-charging modes (see details in Note S1). To be consistent, we follow the terms used by the authors and label those data from the four batches of tests as Batches 1, 2, 3, and 4, in turn. Often a charging protocol includes a wide range of charging rates and is not convenient for analysis. We define an average charging rate c as

$$c = \frac{1}{\psi}\int_0^{\psi} C_r(S_c)\mathrm{d}S_c,$$

where ψ is the state of charge at the end of fast-charging, and $C_r(S_c)$ is the prescribed charging rate. A total of 169 batteries were all discharged with the same CC-CV profile at 4 C to 2.0 V with a current cutoff of C/50, in which the average discharging rate mostly lower than the average charging rate, so batteries' cycle life performances are mainly exacerbated as a result of the fast-charging process.

During charge-discharge cycling of LIBs, degradation of electrochemical performance is reflected in the capacity fading. As shown in Fig. 2a, along with gradual capacity loss, there is an accelerated capacity drop as cycles proceed. The end-of-life of LIBs—once the capacity retention reaches a specified value—corresponds to the number of cycles at that point. Following the suggestion of the authors, the end-of-life of the LFP/graphite LIBs is commonly defined as serving cycles from its 100% capacity retention to its 80% capacity remaining. In what follows, we refer to the end-of-life as N.

We firstly examine c as a function of cycle number (N) in Fig. 1c. Regardless of the rather scattered data, there is a clear trend between the rapid decay of N with increasing c. An analogy of the cycle-life law is well-known in structural materials, the stress-cycle number relationship named the *S*-*N* curve or the Wohler-Basquin curve [6,7]. Therefore, we introduce for batteries under fast-charging mode a cycle-life law in the form of

$$c = c_0 N^{\,b}, \tag{1}$$

where c_0 is a limiting charging rate, and b is a material constant. Physically, one may consider c_0 as a limiting charging rate that a battery fails after one cycle.

We show in Fig. 1c the prediction using $c_0 = 45.5$ and $b = -0.33$ from experimental data in Batch 1. The same parameters also well capture the *c*-*N* relationship of batteries in Batches 3 and 4. A different set of parameters, $c_0 = 38.8$ and $b = -0.33$, fit the experimental data of Batch 2 better. This discrepancy may be due to different batches of samples used in Batch 2. As illustrated in the voltage-capacity curve in Fig. 2b, the voltage from Batch 2 is apparently below those of the other three batches. Similar to what we see from the *S*-*N* curves of materials of the same type, microstructures and processing of materials may influence their power-law fatigue behavior by altering those parameters. The batch-dependent behavior of batteries is hence not out of the line with the broad observations of fatigue in most engineering materials.

We apply Eq. (1) to other commercial LIBs and experimental data from different research groups, as seen in Fig. 1d. LIBs of distinct electrodes, the NMC/graphite LIBs (blue), the NCA/graphite LIBs (red), and the LFP/graphite LIBs (black) are shown. With $c_0 = 19.9$, $b = -0.44$ and $c_0 = 4.76 \times 10^5$, $b = -1.87$ for the NMC/graphite LIBs (blue line) and the NCA/graphite LIBs (red line), respectively, Eq. (1) captures both types of batteries well. For the LFP/graphite

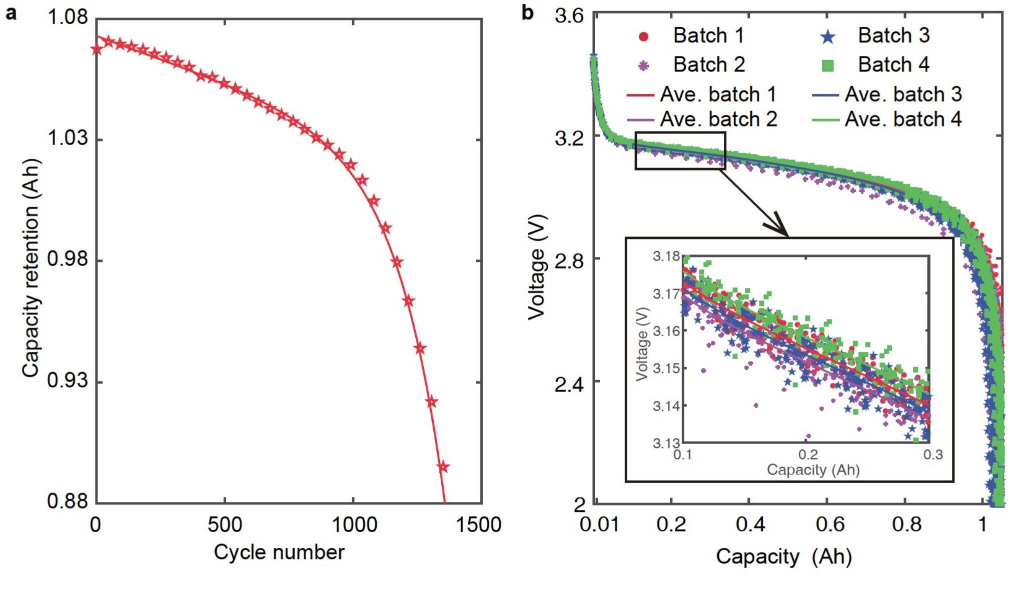

Figure 2 Capacity retention. **a** A typical capacity retention-cycle life curve from Severson et al. [30]. **b** Voltage-capacity of all 169 cells during discharging (at 4 C rate) for the first cycle from experiments. Symbols: data from Severson et al. [30,31]; solid lines: the averaged voltage-capacity for every batch.

LIBs tested, their electrodes are the same as those tested by Severson et al. [30,31], and we used the same parameters $c_0 = 45.5$, $b = -0.33$ and they predict well the degradation of the LFP/graphite LIBs reported by other research groups [32-37].

3. Mechanical mechanisms of fatigue by fast-charging in LIBs

To shed light on the physical origin of the power-law degradation given in Eq. (1), we performed an electro-chemo-mechanical coupling model to examine the evolution of stress in electrode materials at different S_c. There involves the complex electrochemical and mechanical process in a LIB during charging and discharging, as seen in Fig. 3. It is noted that while both charging and discharging may impact the cycle life of batteries, existing experiments are for fast-charging induced damage. We, therefore, zero in on research on batteries during fast-charging, although the following electro-chemo-mechanical coupling model can be applied to both charging and discharging.

3.1 Electro-chemo-mechanical coupling

We are interested in the stress evolution during fast-charging, which involves the electro-chemo-mechanical coupling process including charge conversion (Eqs. (S1) and (S2) in Table S1), mass conservation (Eqs. (S3) and (S4) in Table S1), and electrochemical reaction (Eqs. (S8)-(S10) in Table S1). For lithium diffusion induced stress in active material particles, we consider the most commonly seen structures of active materials composed of particles and consider a particle of radius R. When an active material is subject to charge, the following governing equations summarized in Table S1 should be satisfied:

(1) charge conservation in both solid and liquid phases (Eqs. (S1) and (S2));

(2) diffusion equation of Li and Li-ions (Eqs. (S3) and (S4));

(3) mechanical equilibrium (Eq. (S5));

(4) stress-strain relationships (Eq. (S6));

(5) kinematics (Eq. (S7));

(6) bulter-Volmer equation (Eq. (S8));

(7) equations for open circuit potential in both cathode and anode (Eqs. (S9) and (S10)).

The coupled electro-chemo-mechanical equations are solved by developing a numerical platform based on the LIONSIMBA toolbox [38]. Complete definitions of all related parameters used in Eqs. (S1)-(S10) are tabulated (see Table S2). The values of parameters involved in the electro-chemo-mechanical model either come from the references or are acquired by fitting the tested discharged voltage-time curve in LIBs. Taking the number 1 cell listed in Table S5 for demonstration, the model, fed with the given parameters in Table S2, can capture well the experimental curve in Fig. 3b. The same set of parameters is used for batteries in one batch. For different batches, in order to capture the capacity-voltage curve shown in Fig. 2b, κ_{eff} changes correspondingly, and is 0.25 in Batch 2, 0.65 in Batch 3, and 0.85 in Batch 4.

3.2 Stress and charging rate

The cathode electrode can experience more serious stress evolution (even up to several hundred MPa) at high charging rate conditions because of its poor diffusion performance [39-41]. The large stress status can lead to significant structural failure and greatly influence the cycle-life performance. As active materials in both electrodes are particles, as illustrated in Fig. 3a, we then calculate the stress evolution of such particles in the cathode during a charging-discharging cycle. For the four typical charging protocols of C_r versus S_c

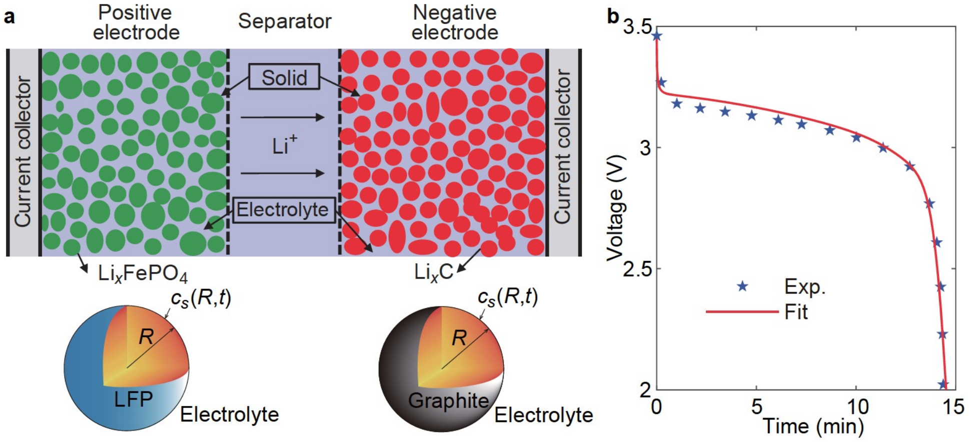

Figure 3 Schematic of the electro-chemo-mechanical coupling process in active materials. **a** An illustration of the LFP/graphite cell electro-chemo-mechanical model. **b** Parameter calibration by fitting the voltage-time curve at a constant discharge rate $C_r = 4$ C.

adopted by Severson et al. [30,31], we check in Fig. 4 the σ_θ evolution at the outer surface of the cathode particle during a full charging and discharging cycle. Note there are 169 independent simulations in order to match all tests, and here we show four characteristic charging protocols (see Fig. 4a), which represent the four batches. Due to the difference in charging, stress evolution in the particle material of the cathode differs dramatically, as demonstrated in Fig. 4b. Lithium concentration and the stress contour in particles of the cathode are shown in Fig. 4c. We show in Fig. 4d the maximum σ_θ during charging, which is also the maximum principle stress, from a total of 169 calculations and their corresponding cycle life from experiments. Regardless of the significant difference in charging protocol, there is a clear trend of $\sigma_\theta = \sigma_0 N^d$, for σ_0 and d being two constants. The same trend is seen if we use either hydrostatic stress p (positive in tension) or shear stress τ. Indeed, the other two principal stress components follow $\sigma_2 = \sigma_1 = \sigma_\theta$ and $\sigma_3 \approx 0$ in spherical particles, and we have by definition, $p = \frac{\sigma_1+\sigma_2+\sigma_3}{3} = 2\sigma_\theta / 3$, and $\tau = \frac{1}{2}\left|\sigma_1 - \sigma_3\right| = \frac{1}{2}\sigma_\theta$. In the fast-charging process, active materials subject to higher stress are prone to initiate microcracks and play a key role in the capacity fade in LIBs.

4. Machine learning based cycle-life prediction

Regardless of the complexity arising from both the large span of temporal and spatial scales and the coupling of multi-mechanisms, we have shown a reliable relationship between cycle life and charging rate based on comprehensive experiments on commercial batteries performed by several groups. There remain further challenges if we examine the cycle life of a batch of as-received cells. They are the same from the perspective of a manufacturer, although customers often find cells ending up with different cycle lives. Given the machine learning (ML) method's capability for extracting the prominent feature from big data accounting for nonlinear mechanical behavior, there is a surge of interest in employing the ML method for the safety assessment of batteries. Severson et al. [30,31,42-44] developed the full data-driven prediction model of LIBs. These developments showed, in the absence of physical augment, full data-driven learning can supply accurate and robust predicting results at the price of a sufficient number of initial cycles, often about tens to nearly one hundred. With the *c*-*N* relationship of Eq. (1) revealed here, we demonstrate here that a PA-ML algorithm is far more efficient: by fed with information of the first charging-discharging cycle of a cell, and the developed PA-ML algorithm predicts the life of the cell with higher fidelity.

4.1 PA-ML algorithm

We consider two essential mechanisms accounting for the cycle life of an arbitrary LIB: a general law governing the history-dependent degradation mechanism of batteries and the specificities characterizing the battery. Therefore, we decompose the cycle life of the battery N by accounting for the two factors:

$$N = f\left(\xi_1, \xi_2, \cdots, \xi_M\right) \cdot g(\omega_1, \omega_2, \cdots, \omega_L), \tag{2}$$

where f describes the influence of M degradation factors $(\xi_1, \xi_2, \cdots, \xi_M)$, and g has L features $(\omega_1, \omega_2, \cdots, \omega_L)$ associated with the specific battery. We now focus on the fast-charging induced capacity fading in LIBs. When charging rate is used as the governing variable accounting for degradation, the degradation function f is in the form of $f(c) = \left(c / c_0\right)^{1/b}$, and consequentially, we have the value of g from $g = \frac{N}{f(c)}$. Alternatively, if we adopt the maximum principal stress as the single variable of f and implement the stress-cycle life relationship shown in Fig. 4d, we have $f(\sigma) = \left(\sigma / \sigma_0\right)^{1/d}$ and $g = \frac{N}{f(\sigma)}$.

From the typical multi-stage charging protocol and its corresponding voltage-S_c curve shown in Fig. 1a and b, along with previous explorations [30], we consider a total of 17 specific features of a cell, and the whole information is given in Note S2. To find an optimal subset out of those candidate features, we adopt the stepwise forward selection method based on prediction performance [45], and identify eight features (as detailed in Note S2) as inputs of $g(\omega_1, \omega_2, \cdots, \omega_L)$ showing great predictability on the cycle life of LIBs. The eight features are (1) fast-charging time till $S_c = 80\%$ (T_c), (2) standard deviation (STD) of voltage during a complete charging (V_c), (3) STD of current during a complete charging (I_c), (4) STD of voltage during constant current discharging (V_d), (5) ratio between the normalized C_m and degradation factor ($C_{md1}(c)$ when charge is used as the factor, and $C_{md2}(\sigma)$ for stress), (6) constant voltage discharging time (T_d), (7) initial resistance (R_r), and (8) measured maximum capacity (C_m), respectively. The values of these eight features of all 169 tests are also given in Table S5. For this particular cycle-life prediction, we employed five different data-driven methods to examine their predictability of $g(\omega_1, \omega_2, \cdots, \omega_8)$, including the support vector regression (SVR) with radial basis function (RBF) kernel, Gaussian process regression (GPR), the gradient boosted regression trees (GBRT), random forest (RF), and the artificial neural networks (ANNs) with three kinds of hidden layers (ANN-1, ANN-2, ANN-3). Three commonly used error criteria, to wit RMSE, MAPE, and MAE,

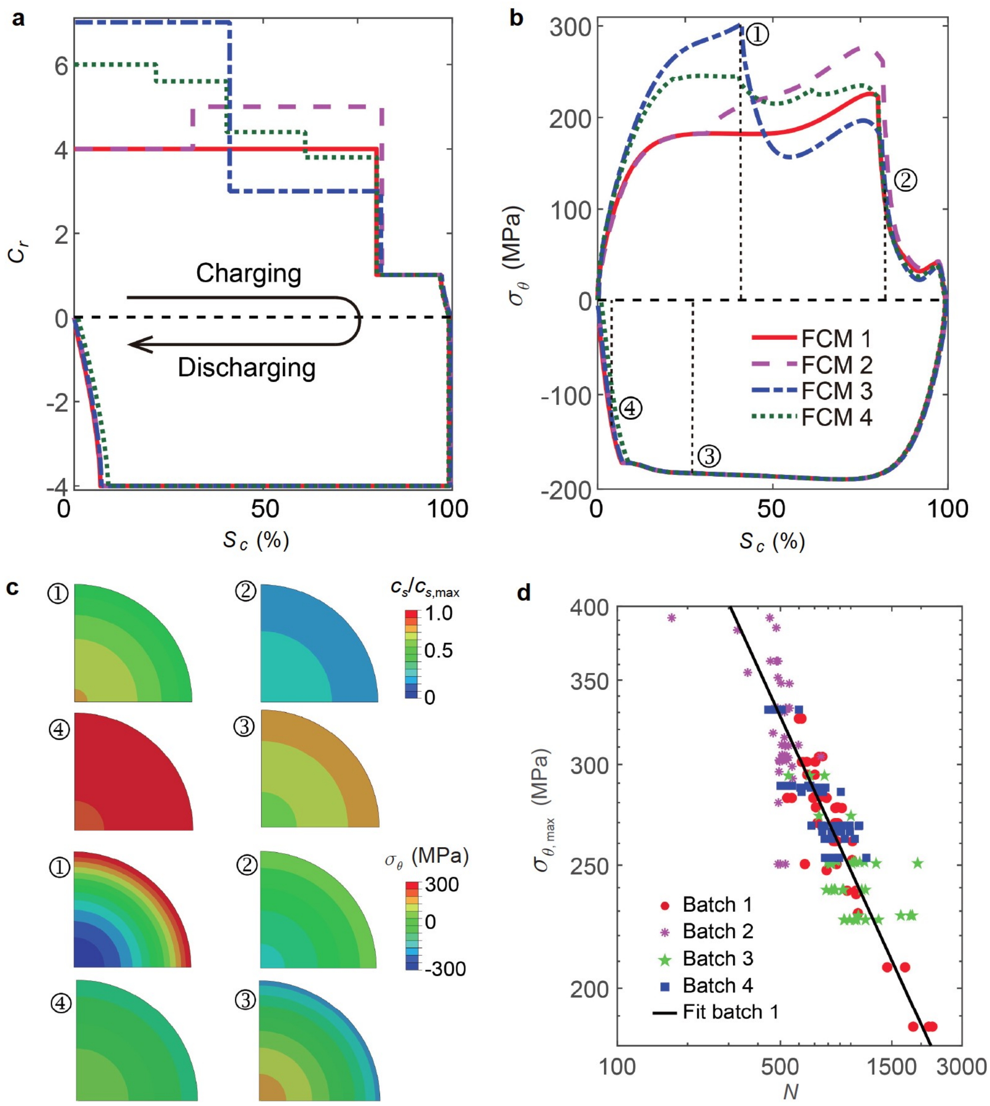

Figure 4 Correlation of stress with cycle number N in electrode materials during fast-charging. **a** Four typical fast-charging modes (see Note S1). **b** Evolution of circumferential stress σ_θ at the outer surface of a cathode particle during a full cycle. **c** Lithium concentration and σ_θ contours at different charging and discharging status keyed in **b**. **d** Maximum σ_θ from 169 calculations versus the corresponding cycle number N from tests (see Table S5). The solid curve is a fitting using $\sigma_\theta = \sigma_0 N^d$, where $\sigma_0 = 4033$, $d = -0.4$.

are used to evaluate their performance. The definitions are detailed here: (1) the root mean squared error, RMSE $= \sqrt{\frac{1}{n}\sum_{i=1}^{n}(y_i - \widehat{y}_i)^2}$; (2) the mean absolute percentage error, MAPE $= \frac{100\%}{n}\sum_{i=1}^{n}\left|\frac{y_i - \widehat{y}_i}{y_i}\right|$; and (3) the mean absolute error, MAE $= \frac{1}{n}\sum_{i=1}^{n}\left|y_i - \widehat{y}_i\right|$. Here y_i and $\widehat{y}_i$ are the observed and predicted cycle lives, respectively. Among the 169 tested batteries, we select randomly two third of the tests (113) as the training dataset and the remaining 56 tests as the prediction dataset, from which we obtain one value of RMSE, MAPE, and MAE for each training method. By repeating the process independently for 50 times, the averaged RMSE, MAPE, and MAE for each of the seven training methods are obtained and shown in Fig. 5. According to the predictions of the five models to $g = \frac{N}{f(c)}$ in Fig. 5a-c and to $g = \frac{N}{f(\sigma)}$ in Fig. 5e-g, the SVR model outperforms the others and has smaller RMSE, MAE, and MAPE, and we employ the SVR model for further exploration.

The statistical dependence between each feature with the value of the specific function g is illustrated by their Spearman correlation coefficients. In Fig. 5d, the Spearman correlation shows a trending upward of g on V_c, I_c, and V_d when the value of g is calculated using $g = \frac{N}{f(c)}$. Figure 5h

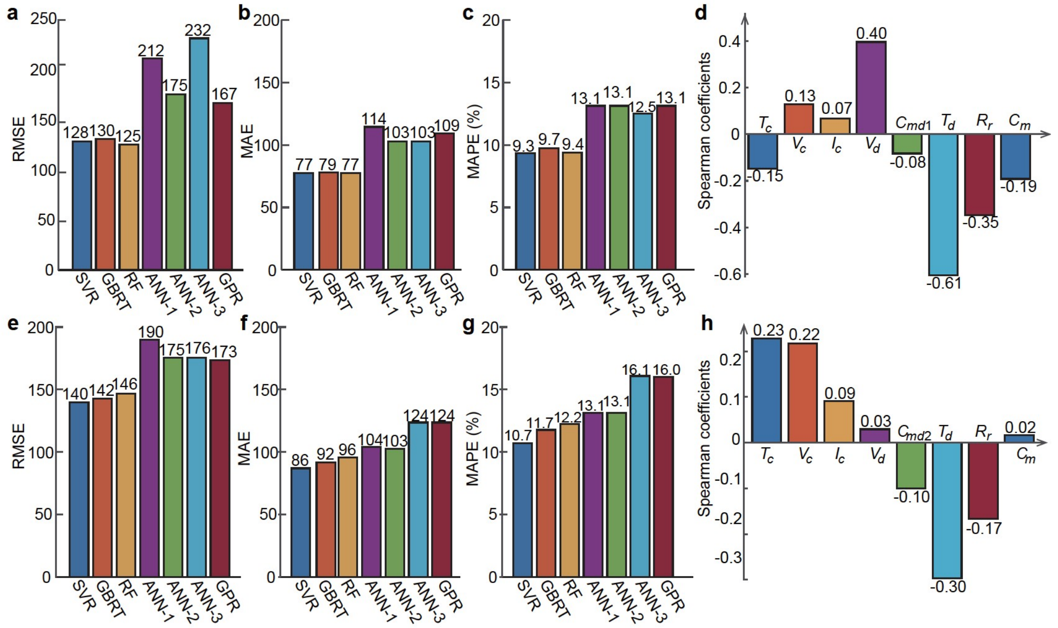

Figure 5 Predictability of data-driven models. **a-c** Error parameters to examine the predictability of seven data-driven models to $g = \frac{N}{f(c)}$: **a** RMSE, **b** MAE, and **c** MAPE. **e-g** Predictions of seven data-driven models to $g = \frac{N}{f(\sigma)}$: **e** RMSE, **f** MAE, and **g** MAPE. The Spearman coefficients of the selected eight specific features (see Note S2) when the value of the specific function g of each test is derived from **d** $g = \frac{N}{f(c)}$ and **h** from $g = \frac{N}{f(\sigma)}$.

suggests trending downward of g on C_{md}, T_d, and R_r when $g = \frac{N}{f(\sigma)}$. The trend of T_c and C_m are distinct, as seen in Fig. 5d and h. It originates from the fact that T_c is roughly the inverse of c.

4.2 Cycle life predictability

With the 169 tests as the dataset, now each sample contains eight features as input and one output g, and the output may be obtained by using either $g = \frac{N}{f(c)}$ or $g = \frac{N}{f(\sigma)}$ with N from experiments. We apply three data processing methods to verify the predictability of the PA-ML model. In method 1, we consider interval-selected cells in Batches 1 and 2 as the training and prediction dataset, respectively. For method 2, cells in Batches 1 and 2 are used as the training dataset and these in Batch 3 as the prediction dataset; and for method 3, we set cells in Batches 1 to 3 as the training dataset and these in Batch 4 as the prediction dataset. The predicted cycle life from the PA-ML model and those from experiments are shown in Fig. 6. Figure 6a and b shows the correlation between our predictor and the observed cycle life, using the definition of charging rate and the stress for output g, respectively. The coefficient ρ between our predictor and the observed cycle life reaches 0.89 and 0.90, respectively. Especially, for method 3, the training dataset only contains two-step charged LIBs, and the accurate prediction for cycle life of LIBs with four-step charging suggests that the PA-ML model performs well for generalization in terms of charging protocol. As a comparison, the RMSE of the PA-ML model outperforms the other three models. In contrast to Severson's ML model [30] and those hybrid ML models listed in Table S3, which require the first many cycles (about 100) as a prior, our PA-ML model gives accurate prediction based on the very first cycle of a LIB and hence saves experimental time and the real usable cycle-life of LIBs. Further different error indicators (RMSE, MAE, and MAPE) are also used to evaluate the predictive performance of the model (Fig. 6c and d). The predicted results, listed in Tables S3 and S4, convincingly highlight the high accuracy and robust predictability of the PA-ML model for the cycle life prediction of LIBs.

5. Discussions and conclusions

To approach the power-law of charging rate versus cycle numbers using experimental data from commercial batteries, there are several issues that merit further exploration. The first one is regarding the possibility of failure in both anode and cathode materials, in contrast to our attention paid to cathode materials. To address this issue, we also investigate the stress evolution in the graphite anode particle during charging and discharging by adopting the same electro-chemo-mechanical coupling model. We show the maximum

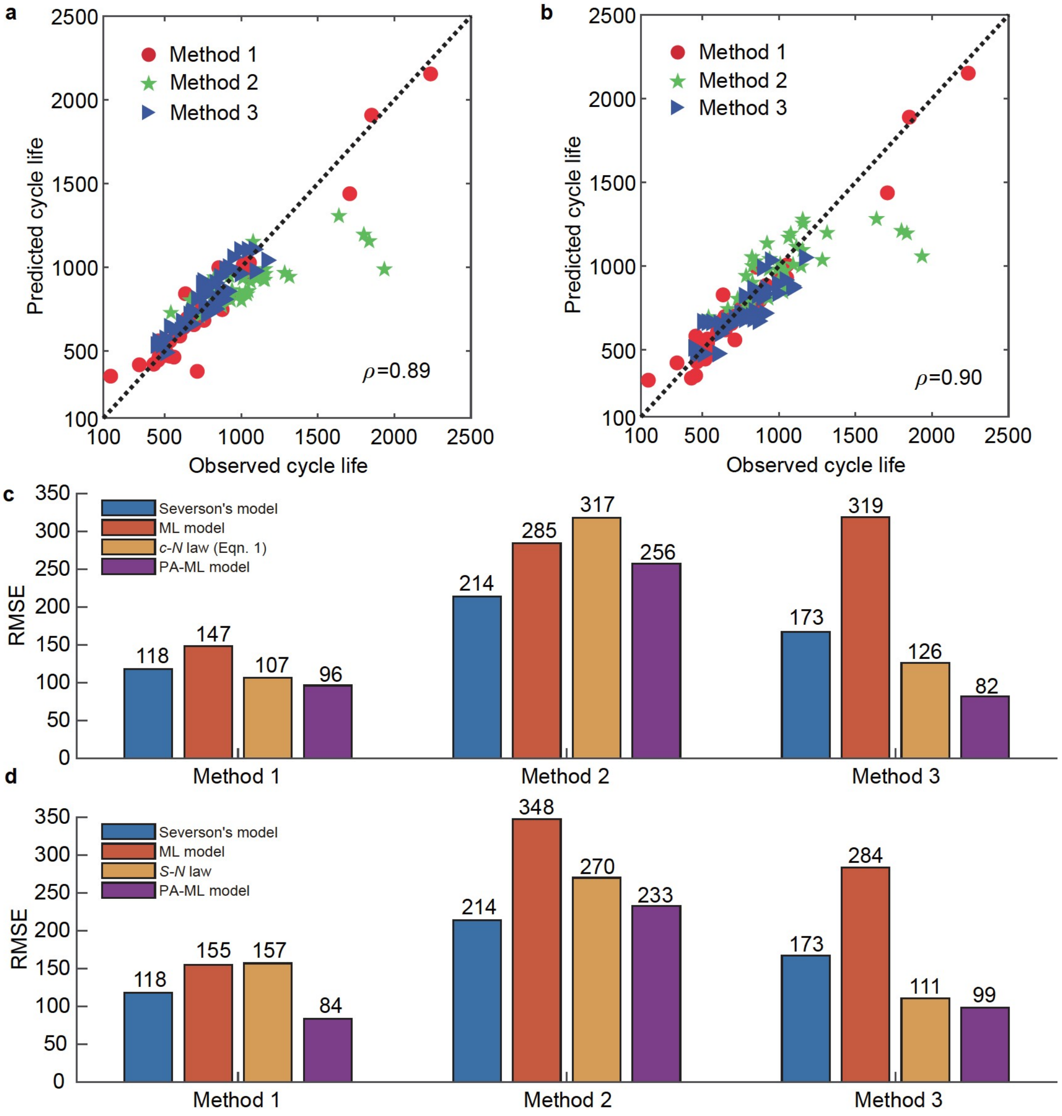

Figure 6 Predictability of the PA-ML model for cycle life of LIBs. The predicted cycle life from the PA-ML cycle-life prediction model versus the observed cycle life using different expressions of the physics law: **a** $g=\frac{N}{f(c)}$, **b** $g=\frac{N}{f(\sigma)}$. **c**, **d** RMSE of our PA-ML in comparison with the other three models corresponding to **a** and **b**, respectively.

stress in graphite anode particles in a cycle in Fig. 7. The magnitude of stresses here, in contrast to those in cathode particles shown in Fig. 4d, is lower by a factor of two to three. It is also worth noting that the power-law relationship is clearly shown in Fig. 4d while data in Fig. 7 are rather scattered. We therefore draw the conclusion that fatigue in the cathode particles in those experiments is responsible for the power-law correlation we suggested here.

A more challenging issue is the applicability of the *c*-*N* curve in real engineering practices. Tests at a laboratory cover a very limited number of charging and discharging history. A customer may use a battery in an unexpected manner, and the SOC window may fall a large span between 0 to 100%, in contrast to a known charging-discharging profile for research. Investigation on this aspect is still lacking. As an off-the-shelf strategy, we may start with constructing a charging spectrum, resembling the stress spectrum commonly used for stress-controlled fatigue, to quantify the accumulative damage due to fast-charging governed fatigue in batteries. The damage due to different levels of charging rate may be approximated by following the conventional Minor's rule for cumulative damage.

To summarize, we reveal a general cycle-life law of commercial batteries under fast-charging protocols based on large-scale and well-documented experiments. The average charging rate c and the resulted cycle life N of LIBs obey $c = c_0N^{b}$, with c_0 being a limiting charging rate and b being anelectrode-dependent parameter. The physical origin of the

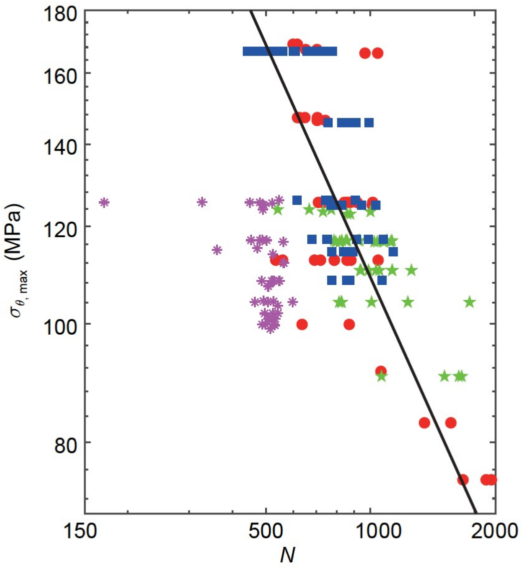

Figure 7 The correlation of stress with cycle life in graphite anode electrode materials during fast-charging. The maximum σ_θ from 169 calculations in graphite anode electrode materials versus the corresponding cycle life N from tests.

power-law degradation is associated with fatigue in active materials subject to high cyclic stress resulting from fast-charging. Initiation of microcracks in active materials of electrodes resulting from cyclic loading gives rise to accumulative damage and exposure of crack surfaces, which in turn facilitates the formation of SEI layers and resultant degradation in LIBs. As further illustrated in Fig. 1, we find that LIBs of the same type of electrodes have a similar value of b. Since c_0 is a limiting charging rate (corresponding to $N = 1$), we prefer to have electrode materials of great c_0 and small b for stable and endurable performance. While the *c*-*N* law supplies two tunable parameters for optimization at the macroscopic level, the Spearman correlation coefficients of the eight features suggest a set of factors for further finer tuning.

With the developed *c*-*N* curve, we further employ a ML method with a physics-augmented algorithm to predict the cycle life of any individual battery. Once the very first cycle performance and the charging profile are available, we can further predict the life of that particular battery with high fidelity. That should be of immediate application for LIBs selection in industries (e.g., EVs) for minimizing battery pack inconsistency during fast-charging. The general *c*-*N* relationship and the PA-ML reported here supply a physically sound approach to realizing health management of LIBs with reliability prediction and quantifiable parameters for further optimization, especially in the ever-growing demand for EVs and battery-based energy storage plants.

Author contributions *Yujie Wei conceived the project and proposed the c-N law; Jici Wen and Yujie Wei developed the theoretical model, Qingrong Zou and Zehui Zhang involved in the theoretical analysis; Qingrong Zou, Jici Wen, and Jian Shi performed the machine-learning based analysis. Yujie Wei, Jici Wen, and Qingrong Zou wrote the draft. All authors analyzed data, discussed the results, and reviewed and edited the manuscript.*

Acknowledgements *Yujie Wei acknowledges support from the National Natural Science Foundation of China (NSFC) Basic Science Center for "Multiscale Problems in Nonlinear Mechanics" (Grant No. 11988102), and Jici Wen thanks for support from NSFC (Grant No. 12002343).*

1 C. Niu, J. Liu, T. Qian, X. Shen, J. Zhou, and C. Yan, Single lithium-ion channel polymer binder for stabilizing sulfur cathodes, Natl. Sci. Rev. **7**, 315 (2020).
2 K. J. Park, J. Y. Hwang, H. H. Ryu, F. Maglia, S. J. Kim, P. Lamp, C. S. Yoon, and Y. K. Sun, Degradation mechanism of Ni-enriched NCA cathode for lithium batteries: are microcracks really critical? ACS Energy Lett. **4**, 1394 (2019).
3 Y. Wang, D. Dang, D. Li, J. Hu, and Y. T. Cheng, Influence of polymeric binders on mechanical properties and microstructure evolution of silicon composite electrodes during electrochemical cycling, J. Power Sources **425**, 170 (2019).
4 M. B. Pinson, and M. Z. Bazant, Theory of SEI formation in rechargeable batteries: Capacity fade, accelerated aging and lifetime prediction, J. Electrochem. Soc. **160**, A243 (2012).
5 S. Suresh, Fatigue of Materials, 2nd ed. (Cambridge University Press, Cambridge, 1998).
6 O. H. Basquin, The exponential law of endurance tests, Am. Soc. Test. Mater. Proc. **10**, 625 (1910).
7 A. Wohler, Versuche über die Festigkeit der Eisenbahnwagenachsen, Z. für Bauwesen **10**, 160 (1860).
8 R. Deshpande, M. Verbrugge, Y. T. Cheng, J. Wang, and P. Liu, Battery cycle life prediction with coupled chemical degradation and fatigue mechanics, J. Electrochem. Soc. **159**, A1730 (2012).
9 L. Yang, N. Li, L. Hu, S. Wang, L. Wang, J. Zhou, W. L. Song, L. Sun, T. S. Pan, H. S. Chen, and D. Fang, Internal field study of 21700 battery based on long-life embedded wireless temperature sensor, Acta Mech. Sin. **37**, 895 (2021).
10 Y. Suo, and F. Yang, One-dimensional analysis of the coupling between diffusion and deformation in a bilayer electrode, Acta Mech. Sin. **35**, 589 (2019).
11 V. A. Sethuraman, V. Srinivasan, A. F. Bower, and P. R. Guduru, *In situ* measurements of stress-potential coupling in lithiated silicon, J. Electrochem. Soc. **157**, A1253 (2010).
12 H. Xie, Y. Kang, H. Song, J. Guo, and Q. Zhang, *In situ* method for stress measurements in film-substrate electrodes during electrochemical processes: Key role of softening and stiffening, Acta Mech. Sin. **36**, 1319 (2020).
13 M. G. Boebinger, D. Yeh, M. Xu, B. C. Miles, B. Wang, M. Papakyriakou, J. A. Lewis, N. P. Kondekar, F. J. Q. Cortes, S. Hwang, X. Sang, D. Su, R. R. Unocic, S. Xia, T. Zhu, and M. T. McDowell, Avoiding fracture in a conversion battery material through reaction with larger ions, Joule **2**, 1783 (2018).
14 J. Wen, Y. Wei, and Y. T. Cheng, Stress evolution in elastic-plastic electrodes during electrochemical processes: A numerical method and its applications, J. Mech. Phys. Solids **116**, 403 (2018).
15 L. Yang, H. S. Chen, H. Jiang, Y. J. Wei, W. L. Song, and D. N. Fang, Failure mechanisms of 2D silicon film anodes: *in situ* observations and simulations on crack evolution, Chem. Commun. **54**, 3997 (2018).
16 K. Guo, W. Zhang, B. W. Sheldon, and H. Gao, Concentration dependent properties lead to plastic ratcheting in thin island electrodes on substrate under cyclic charging and discharging, Acta Mater. **164**, 261 (2019).
17 C. Wang, J. Wen, F. Luo, B. Quan, H. Li, Y. Wei, C. Gu, and J. Li, Anisotropic expansion and size-dependent fracture of silicon nanotubes during lithiation, J. Mater. Chem. A **7**, 15113 (2019).
18 E. Peled, and S. Menkin, Review—SEI: Past, present and future, J. Electrochem. Soc. **164**, A1703 (2017).

19 C. Chen, T. Zhou, D. L. Danilov, L. Gao, S. Benning, N. Schön, S. Tardif, H. Simons, F. Hausen, T. U. Schülli, R. A. Eichel, and P. H. L. Notten, Impact of dual-layer solid-electrolyte interphase inhomogeneities on early-stage defect formation in Si electrodes, Nat. Commun. **11**, 3283 (2020).

20 X. Zhang, Q. J. Wang, K. L. Harrison, S. A. Roberts, and S. J. Harris, Pressure-driven interface evolution in solid-state lithium metal batteries, Cell Rep. Phys. Sci. **1**, 100012 (2020).

21 C. Chen, M. Jiang, T. Zhou, L. Raijmakers, E. Vezhlev, B. Wu, T. U. Schülli, D. L. Danilov, Y. Wei, R. Eichel, and P. H. L. Notten, Interface aspects in all-solid-state Li-based batteries reviewed, Adv. Energy Mater. **11**, 2003939 (2021).

22 K. Turcheniuk, D. Bondarev, V. Singhal, and G. Yushin, Ten years left to redesign lithium-ion batteries, Nature **559**, 467 (2018).

23 P. Simon, and Y. Gogotsi, Perspectives for electrochemical capacitors and related devices, Nat. Mater. **19**, 1151 (2020).

24 C. P. Grey, and D. S. Hall, Prospects for lithium-ion batteries and beyond—A 2030 vision, Nat. Commun. **11**, 6279 (2020).

25 G. Qian, J. Wang, H. Li, Z. F. Ma, P. Pianetta, L. Li, X. Yu, and Y. Liu, Structural and chemical evolution in layered oxide cathodes of lithium-ion batteries revealed by synchrotron techniques, Natl. Sci. Rev. **9**, nwab146 (2022).

26 V. Sulzer, P. Mohtat, A. Aitio, S. Lee, Y. T. Yeh, F. Steinbacher, M. U. Khan, J. W. Lee, J. B. Siegel, A. G. Stefanopoulou, and D. A. Howey, The challenge and opportunity of battery lifetime prediction from field data, Joule **5**, 1934 (2021).

27 J. Neubauer, and E. Wood, The impact of range anxiety and home, workplace, and public charging infrastructure on simulated battery electric vehicle lifetime utility, J. Power Sources **257**, 12 (2014).

28 Y. Liu, Y. Zhu, and Y. Cui, Challenges and opportunities towards fast-charging battery materials, Nat. Energy **4**, 540 (2019).

29 M. Weiss, R. Ruess, J. Kasnatscheew, Y. Levartovsky, N. R. Levy, P. Minnmann, L. Stolz, T. Waldmann, M. Wohlfahrt-Mehrens, D. Aurbach, M. Winter, Y. Ein-Eli, and J. Janek, Fast charging of lithium-ion batteries: A review of materials aspects, Adv. Energy Mater. **11**, 2101126 (2021).

30 K. A. Severson, P. M. Attia, N. Jin, N. Perkins, B. Jiang, Z. Yang, M. H. Chen, M. Aykol, P. K. Herring, D. Fraggedakis, M. Z. Bazant, S. J. Harris, W. C. Chueh, and R. D. Braatz, Data-driven prediction of battery cycle life before capacity degradation, Nat. Energy **4**, 383 (2019).

31 P. M. Attia, A. Grover, N. Jin, K. A. Severson, T. M. Markov, Y. H. Liao, M. H. Chen, B. Cheong, N. Perkins, Z. Yang, P. K. Herring, M. Aykol, S. J. Harris, R. D. Braatz, S. Ermon, and W. C. Chueh, Closed-loop optimization of fast-charging protocols for batteries with machine learning, Nature **578**, 397 (2020).

32 P. Keil, and A. Jossen, Charging protocols for lithium-ion batteries and their impact on cycle life—An experimental study with different 18650 high-power cells, J. Energy Storage **6**, 125 (2016).

33 A. Maheshwari, M. Heck, and M. Santarelli, Cycle aging studies of lithium nickel manganese cobalt oxide-based batteries using electrochemical impedance spectroscopy, Electrochim. Acta **273**, 335 (2018).

34 Y. Preger, H. M. Barkholtz, A. Fresquez, D. L. Campbell, B. W. Juba, J. Romàn-Kustas, S. R. Ferreira, and B. Chalamala, Degradation of commercial lithium-ion cells as a function of chemistry and cycling conditions, J. Electrochem. Soc. **167**, 120532 (2020).

35 Y. Yin, and S. Y. Choe, Actively temperature controlled health-aware fast charging method for lithium-ion battery using nonlinear model predictive control, Appl. Energy **271**, 115232 (2020).

36 R. Mathieu, O. Briat, P. Gyan, and J. M. Vinassa, Comparison of the impact of fast charging on the cycle life of three lithium-ion cells under several parameters of charge protocol and temperatures, Appl. Energy **283**, 116344 (2021).

37 N. Paul, J. Keil, F. M. Kindermann, S. Schebesta, O. Dolotko, M. J. Mühlbauer, L. Kraft, S. V. Erhard, A. Jossen, and R. Gilles, Aging in 18650-type Li-ion cells examined with neutron diffraction, electrochemical analysis and physico-chemical modeling, J. Energy Storage **17**, 383 (2018).

38 M. Torchio, L. Magni, R. B. Gopaluni, R. D. Braatz, and D. M. Raimondo, Lionsimba: A Matlab framework based on a finite volume model suitable for li-ion battery design, simulation, and control, J. Electrochem. Soc. **163**, A1192 (2016).

39 Y. Zheng, Y. B. He, K. Qian, B. Li, X. Wang, J. Li, S. W. Chiang, C. Miao, F. Kang, and J. Zhang, Deterioration of lithium iron phosphate/graphite power batteries under high-rate discharge cycling, Electrochim. Acta **176**, 270 (2015).

40 D. Li, G. Zhu, H. Liu, and Y. Wang, Diffusion-induced stress in commercial graphite electrodes during multiple cycles measured by an in situ method, Micromachines **13**, 142 (2022).

41 S. Kim, J. Wee, K. Peters, and H. Y. S. Huang, Multiphysics coupling in lithium-ion batteries with reconstructed porous microstructures, J. Phys. Chem. C **122**, 5280 (2018).

42 Z. Tong, J. Miao, S. Tong, and Y. Lu, Early prediction of remaining useful life for lithium-ion batteries based on a hybrid machine learning method, J. Cleaner Production **317**, 128265 (2021).

43 S. Shen, V. Nemani, J. Liu, C. Hu, and Z. Wang, in A hybrid machine learning model for battery cycle life prediction with early cycle data: Proceedings of 2020 IEEE Transportation Electrification Conference & Expo (IEEE, Chicago, 2020), pp. 181-184.

44 J. Wen, Q. Zou, and Y. Wei, Physics-driven machine learning model on temperature and time-dependent deformation in lithium metal and its finite element implementation, J. Mech. Phys. Solids **153**, 104481 (2021).

45 S. Derksen, and H. J. Keselman, Backward, forward and stepwise automated subset selection algorithms: Frequency of obtaining authentic and noise variables, Br. J. Math. Statistical Psychol. **45**, 265 (1992).

商业锂电池充电倍率与循环寿命的标度律

温济慈, 邹庆荣, 张泽卉, 石坚, 魏宇杰

摘要 商用锂电池的健康管理目前存在大量亟待解决的问题，其中循环寿命的有效预测是电池管理系统的核心目标. 本文通过利用商业锂电池不同快充倍率下循环寿命的实验结果，发现并提出了锂电池等效快充倍率c与循环寿命N之间的标度律关系，$c = c_0N^b$（即c-N准则），其中c_0表示电极材料极限充电倍率，b是与电池材料相关的常数. 这一c-N准则，类似于固体材料疲劳中所周知的S-N曲线，适用于不同类型的商业锂电池，并通过已有的文献数据获得了验证. 结合c-N准则和机器学习方法，我们发展了一种物理增强的机器学习模型，基于前面提出的c-N准则，使用首圈的充放电测试即可实现对电池循环寿命的高精度预测. 这一工作为锂电池循环寿命预测、健康管理和锂电池的优化提供了基于力学原理的新思路.